The Astrophysical Journal, 746:157 (13pp), 2012 February 20 doi:10.1088/0004-637X/746/2/157

RELATIVISTIC MODEL ON PULSAR RADIO EMISSION AND POLARIZATION

D. Kumar and R. T. Gangadhara
Indian Institute of Astrophysics, Bangalore-5600034, India; dinesh@iiap.res.in, ganga@iiap.res.in
Received 2011 September 4; accepted 2011 December 5; published 2012 February 2

ABSTRACT

We have developed a relativistic model for pulsar radio emission and polarization by taking into account a detailed geometry of emission region, rotation, and modulation. The sparks activity on the polar cap leads to plasma columns in the emission region and modulated emission. By considering relativistic plasma bunches streaming out along the rotating dipolar field lines as a source of curvature radiation, we have deduced the polarization state of the radiation field in terms of the Stokes parameters. We have simulated a set of typical pulse profiles and analyzed the role of viewing geometry, rotation, and modulation in the pulsar polarization profiles. Our simulations explain most of the diverse behaviors of polarization generally found in pulsar radio profiles. We show that both the "antisymmetric" and "symmetric" types of circular polarization are possible within the framework of curvature radiation. We also show that the "kinky" nature in the polarization position angle traverses might be due to the rotation and modulation effects. The phase lag of the polarization position angle inflection point relative to the phase of core peak depends upon the rotationally induced asymmetry in the curvature of source trajectory and modulation.

Key words: polarization – pulsars: general – radiation mechanisms: non-thermal

1. INTRODUCTION

Even though pulsars were discovered more than four decades ago, their radio emission process is still not completely understood. The very high degree of linear polarization and systematic polarization position angle (PPA) swing of pulsar radiation have been naturally invoked in curvature radiation (Sturrock 1971; Ruderman & Sutherland 1975). In the framework of curvature radiation models the radio emission is believed to be emitted by relativistic plasma streaming "force freely" along the open field lines of the super-strong magnetic field, the geometry of which is assumed to be predominantly dipolar. In the non-rotating approximation, the velocity of relativistic plasma will be parallel to the tangents of the field lines with which they are associated, hence, emitted radiation is beamed in the direction of field line tangents. In the rotating vector model (RVM), as the pulsar rotates, the observer sight line encounters different dipolar field lines, resulting in the "S"-shaped PPA swing, which is more or less determined by the geometry of the emission region (Radhakrishnan & Cooke 1969; Komesaroff 1970).

Pulsar radio emission is believed to come from mainly open dipolar field lines that lie within the polar cap region. The shapes of individual pulses indicate that the entire polar cap might not be radiating uniformly. The sub-pulse modulation can be explained by the idea of isolated sparks on the polar cap (e.g., Ruderman & Sutherland 1975; Cheng & Ruderman 1980). Pulsar average profiles resulting from the summation of several hundreds of individual pulses have well-defined shapes and in general are made up of many components. Phenomenologically, pulsar emission is recognized as central "core" emission arising from the region near the magnetic pole and "cone" emission arising from concentric rings around the pole (e.g., Rankin 1983, 1990, 1993; Mitra & Deshpande 1999; Gangadhara & Gupta 2001; Mitra & Rankin 2002). However, there are some contrary arguments that the emission is "patchy" (Lyne & Manchester 1988).

Since pulsars are fast spinning objects, rotation effects such as aberration, retardation, and polar cap currents are believed to strongly influence their emission. For an inertial observer, in addition to intrinsic velocity along the field line tangents, particles will have a corotation velocity component. Therefore, in the inertial observer frame, the net velocity of particles will be offset from the field line tangents with which they are associated; hence, the emission will be aberrated in the direction of pulsar rotation. Taking rotation into account, Blaskiewicz et al. (1991), hereafter BCW (1991), proposed a relativistic pulsar polarization model. By assuming a constant emission altitude r across the whole pulse, they predicted that the midpoint of the intensity profile shifts to the earlier phase by $\sim r/r_{\rm LC}$ with respect to the fiducial phase, whereas the PPA inflection point shifts to a later phase by $\sim 3r/r_{\rm LC}$. The parameter $r_{\rm LC} = cP/2\pi$ is the light cylinder radius, where c is the velocity of light and P is the pulsar rotation period. Further, they showed that the intensity on the leading side becomes stronger than that on the trailing side due to rotation; this has strong observational support (Lyne & Manchester 1988). Hibschman & Arons (2001) further improved the relativistic RVM model by taking into account the induced magnetic field due to polar cap currents. Dyks (2008) presented a simpler derivation in which he reproduced the BCW (1991) prediction. Following these deductions, Thomas & Gangadhara (2010) estimated the absolute emission altitudes of a few pulsars. The asymmetry in the phase location of conal components with respect to core has been interpreted in terms of rotation effects such as aberration and retardation phase shifts (Gangadhara & Gupta 2001; Gupta & Gangadhara 2003; Dyks et al. 2004; Gangadhara 2005; Krzeszowski et al. 2009).

By solving the equation of motion, Thomas & Gangadhara (2007) also predicted that the emissions on the leading side dominate those on the trailing side due to rotation-induced asymmetry in the curvature of the trajectory of bunches. Dyks et al. (2010) analyzed the influence of rotation on the shape of pulse profiles of millisecond pulsars and identified two opposing effects of corotation: (1) the caustic enhancement of the trailing side emission due to squeezing into a narrower component and (2) the weakening of the trailing side caused by the smaller curvature of source trajectories. Thomas et al. (2010) discussed the significance of geometric and rotation effects to the pulsar radio profiles and interpreted the asymmetry in the pulsar radio profiles, particularly "partial cones" (which were first termed by Lyne & Manchester 1988) in terms of the rotation effects. These

are notable for their highly asymmetric average intensity profiles and PPA traverses, wherein one side of a double component conal profile is either missing or significantly suppressed, and the PPA inflection point lies well toward the trailing side.

Among the several theoretical problems related to exploring the pulsar radio emission mechanism is the mostly unexplained observational fact of the high degree of circular polarization and its very diverse behavior. By analyzing average pulsar profiles, Radhakrishnan & Rankin (1990) identified two types of circular polarization, namely, "antisymmetric," where the circular polarization changes its sense near the center of the pulse profile, and "symmetric," where the circular polarization will have the same sense across the whole pulse profile. In the case of pulsars with antisymmetric type, they found a strong correlation between the sense reversal of circular polarization and the PPA swing, and speculated that it could be a geometric property of emission mechanism. Han et al. (1998) noticed that circular polarization is common in pulsars but diverse in nature, and even though it is generally strongest in the central or "core" regions, it is by no means confined to central regions. They found a strong correlation between the sense of circular polarization and the PPA swing in the double-conal pulsars and no correlation between the sense reversal of circular polarization near the center of pulse profiles and the PPA swing in the pulsars with the antisymmetric type of circular polarization. Further, You & Han (2006) reconfirmed these investigations with larger data.

There are two probable origins of circular polarization proposed for the pulsar radiation; it is either intrinsic to the emission mechanism (e.g., Michel 1987; Gil & Snakowski 1990a, 1990b; Radhakrishnan & Rankin 1990; Gangadhara 1997, 2010) or generated by the propagation effects (e.g., Cheng & Ruderman 1979; Melrose 2003). Gil et al. (1993) modeled the single-pulse polarization characteristics of pulsar radiation and argued that the strong sense reversing circular polarization is a natural feature of curvature radiation. Cheng & Ruderman (1979) suggested that conversion of linear polarization to circular polarization is possible due to the expected asymmetry between the positive and negative charged components of magneto active plasma in the far magnetosphere. On the other hand, Kazbegi et al. (1991) argued that the cyclotron instability, rather than the propagation effect, is responsible for the circular polarization of pulsar radiation. By considering the rotation of the magnetosphere, Lyubarskii & Petrova (1999) showed that the induced wave mode coupling in the polarization-limiting region can result in circular polarization in linearly polarized normal waves. Melrose (2003) reviewed the properties of intrinsic circular polarization and the circular polarization due to cyclotron instability, and discussed the circular polarization due to propagation effects in an inhomogeneous birefringent plasma.

Recently, Gangadhara (2010) developed a curvature radiation model by considering the detailed geometry of the emission region in the non-rotating pulsar approximation. His results support the fact that the circular polarization survives only when there is a sufficient gradient in the sub-pulse modulation, and the antisymmetric circular polarization is part of the intrinsic nature of the curvature radiation. He confirmed the Radhakrishnan & Rankin (1990) correlation between the sense reversal of circular polarization and the PPA swing. He also showed that the sense reversal of circular polarization is by no means confined to central core regions.

Although extensive pulsar polarimetric studies are available, pulsar emission and polarization are not well understood due to their diverse nature. Despite rotation effects such as aberration and retardation being strongly believed to influence the pulsar radio profiles, a complete polarization model including rotation effects has not been attempted in the literature. In the work of Thomas & Gangadhara (2007) and Thomas et al. (2010), Dyks et al. (2010) modeled only the total intensity and left the polarization part untouched. On the other hand, relativistic models proposed by BCW (1991), Hibschman & Arons (2001), and Dyks (2008) deal with PPA only, leaving out the linear polarization. Further, in their models, emission from the points at which bunch velocity exactly aligns with the sight line is only considered, and the emissions from the neighboring points at which velocity lies within $\sim 1/\gamma$ with respect to sight line are not considered. Such emission does influence PPA swing if modulated, as we show in our model.

For the first time, we have developed a complete polarization model by taking into account a detailed geometry of emission region, rotation effects, and modulation. We adopt the features of curvature radiation and incorporate the Gaussian sub-pulse modulation. At any instant of time, the observer tends to receive the incoherent curvature radiation from a modulated beaming region, which constitutes a small flux tube of dipolar field lines. Based on simulated profiles, we discuss the combined effect of rotation and modulation on the typical pulsar radio profiles. We describe the asymmetry in the pulsar radio profiles in terms of combined effects of viewing geometry, rotation, and modulation. In Section 2, we derive the expressions for the radiation electric field in the frequency domain and the Stokes parameters. We present a simulation of typical pulse profiles in Section 3, the discussion in Section 4, and the conclusion in Section 5.

2. POLARIZATION STATE OF THE RADIATION FIELD

Relativistic plasma streaming "force freely" along the super-strong dipolar magnetic field lines emits beamed curvature radiation. The curvature radiation model requires efficient plasma bunching to account for the very high brightness temperature of the pulsar radio emission, wherein plasma bunches of a size smaller than or equal to the radiation wavelength can emit coherently (e.g., Sturrock 1971; Ruderman & Sutherland 1975; Cheng & Ruderman 1980). In our model, we treat the plasma bunch as a single particle of charge $q = Ne$, where e is the electronic charge and N is the number of particles. In this paper we alternatively use source, particle, or plasma bunch as the source of radio emission but all three terms mean the same thing. The emissions from different bunches become incoherent, as such emissions do not bear any phase relation.

Consider an inclined and rotating magnetic dipole in the inertial observer's frame (IOF), a stationary Cartesian coordinate system—XYZ with neutron star center O as the origin, as shown in Figure 1. The angular velocity $\mathbf{\Omega}$ is considered along the positive Z-axis, and the magnetic axis $\hat{m}$ is inclined by an angle α with respect to $\mathbf{\Omega}$. Consider a radiation source S constrained to move along the rotating field line f. The velocity $\mathbf{v}$ of the source is given by

$$\mathbf{v} = \kappa c \hat{b} + \mathbf{\Omega} \times \mathbf{r}, \tag{1}$$

where $\hat{b}$ is the unit tangent vector to the field line and $\mathbf{r}$ is the position vector of the source; their expressions are given in Gangadhara (2010). The parameter κ specifies the speed of the source along the field line as a fraction of the speed of light c. The first term on the right-hand side of Equation (1) is the

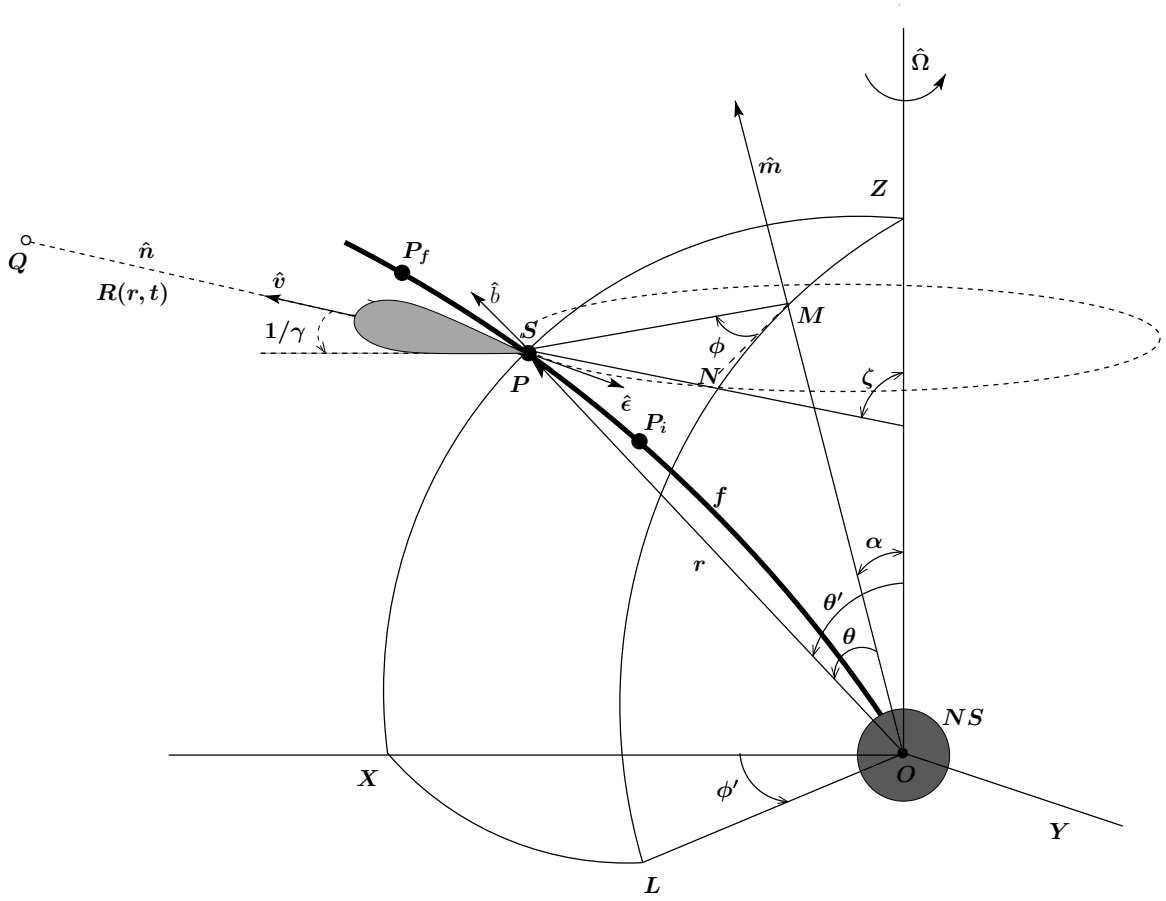

Figure 1. Geometry of radiation emission from a relativistic source S accelerated along a rotating field line f (thick curve) in a stationary inertial frame XYZ with neutron star center O as the origin. $\hat{\Omega}$ is the rotation axis, $\hat{m}$ is the magnetic axis, and $\hat{b}$ is the field line tangent. The rotation direction is $\hat{\epsilon}$, and the net velocity is $\hat{v}$. The observer's sight line $\hat{n}$ lies in the fiducial plane (XZ-plane). ZPX, ZML, and XL are the great circles centered on O. The observation point Q is at a distance R from the emission point P.

velocity in the corotating frame and is in the direction of the associated field line tangent, and the second term is corotation velocity. Hence, the velocity of the source is offset from the field line tangent with which it is associated and is aberrated in the direction of pulsar rotation. The parameter κ can be deduced from Equation (1) by assuming $|\mathbf{v}| = \beta c$,

$$\kappa = \sqrt{\beta^2 - \left(\frac{\Omega r}{c}\right)^2 \sin^2\theta' \sin^2\Theta} - \frac{\Omega r}{c}\sin\theta'\cos\Theta, \quad (2)$$

where $\beta = \sqrt{1-1/\gamma^2}$, γ is the Lorentz factor of the source, θ' is the angle between $\mathbf{r}$ and $\mathbf{\Omega}$, and Θ is the angle between $\mathbf{b}$ and the rotation direction $\hat{\epsilon}$. The expressions for θ' and Θ are given in Gangadhara (2005).

The acceleration $\mathbf{a} = d\mathbf{v}/dt$ of source in IOF is given by

$$\mathbf{a} = \frac{(\kappa c)^2}{|\mathbf{b}|}\frac{\partial \hat{b}}{\partial\theta} + \frac{\kappa c^2}{|\mathbf{b}|}\frac{\partial\kappa}{\partial\theta}\hat{b} + 2\kappa c(\mathbf{\Omega}\times\hat{b}) + \mathbf{\Omega}\times(\mathbf{\Omega}\times\mathbf{r}), \quad (3)$$

where we have used the expression of the arc length of the field line $ds = |\mathbf{b}|d\theta = \kappa c dt$, wherein $|\mathbf{b}|$ is the magnitude of the field line tangent and θ is magnetic colatitude. The expression for $|\mathbf{b}|$ is given in Gangadhara (2004).

The first term on the right-hand side of Equation (3) is the acceleration of the bunch due to curvature of the dipolar magnetic field line; this is the only term which exists in the absence of rotation (Gangadhara 2010). The second term is due to a small change in the speed of the bunch due to motion along the field line. The third and last terms are the accelerations due to Coriolis and the Centrifugal forces, respectively.

As the relativistic source accelerates along the rotating field line, it emits curvature radiation whose spectral distribution at the observation point Q is given by (Gangadhara 2010)

$$\mathbf{E}(\mathbf{r},\omega) = \frac{1}{\sqrt{2\pi}}\frac{q e^{i\omega R_0/c}}{R_0 c} \times \int_{-\infty}^{+\infty} \frac{\hat{n}\times[(\hat{n}-\boldsymbol{\beta})\times\dot{\boldsymbol{\beta}}]}{\xi^2} e^{i\omega(t-\hat{n}\cdot\mathbf{r}/c)}dt, \quad (4)$$

where $\hat{n} = \{\sin\zeta, 0, \cos\zeta\}$ is the observer's sight line and $\zeta = \alpha + \sigma$, with σ being the sight line impact angle. The parameters $\boldsymbol{\beta} = \mathbf{v}/c$ and $\dot{\boldsymbol{\beta}} = \mathbf{a}/c$ are the velocity and acceleration of source, respectively. $\xi = 1 - \boldsymbol{\beta}\cdot\hat{n}$, and R_0 is the distance from the neutron star center to the observer.

At any rotation phase $\phi' = \phi'_m$ of the magnetic axis, and for a given emission altitude r, the viewing geometry allows the observer to receive the beamed emission only from a specific region of the pulsar magnetosphere. The observer receives the maximum radiation from the emission point at which $\hat{v}$ and $\hat{n}$ are exactly aligned; we define the corresponding magnetic colatitude $\theta = \theta_0$ and azimuth $\phi = \phi_0$. By considering a slowly rotating (or non-rotating) magnetosphere, Gangadhara (2004) derived the expressions for θ_0 and ϕ_0 as functions of rotation phase $\phi' = \phi'_m$ of the magnetic axis (see Equations (9) and (11)

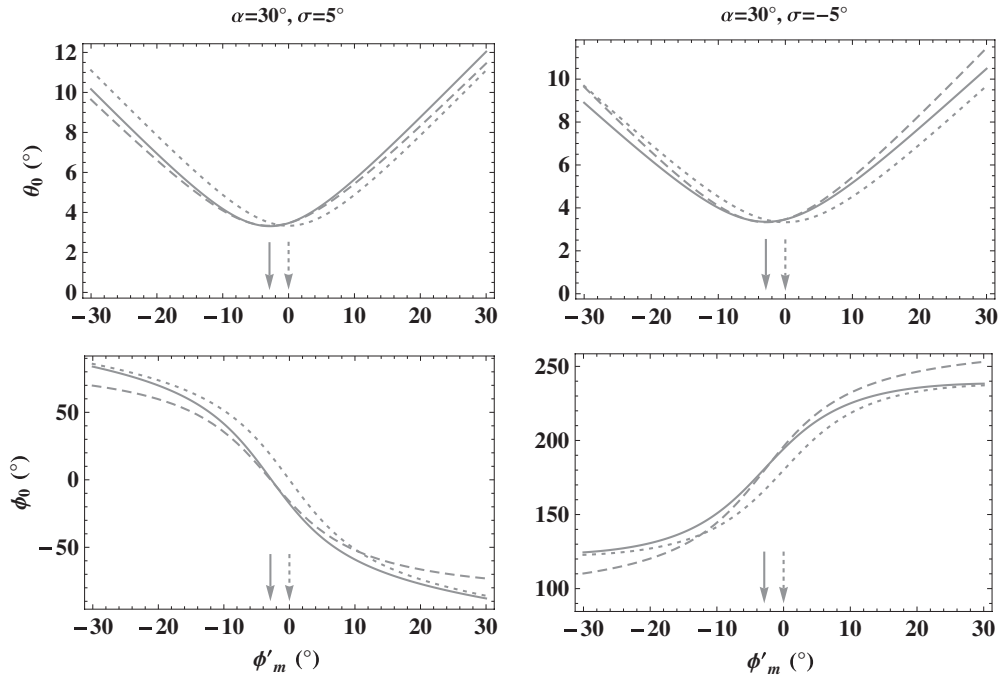

Figure 2. Magnetic colatitude θ_0 and azimuth ϕ_0 of the emission point as functions of rotation phase ϕ'_m in the non-rotating (dotted curves) and rotating (solid curves) cases. The dashed curves are those due to the BCW (1991) model. Here, $P = 1$ s, and $r_n = r/r_{\rm LC} = 0.05$. The dotted and solid arrows in the upper panels represent the location of θ_0 minima, while in the lower panels they show the location of the inflection point of ϕ_0 in the non-rotating and rotating cases, respectively.

in Gangadhara 2004). We solve $\hat{n} \cdot \hat{v} = 1$ numerically to find θ_0 and ϕ_0, as the exact analytical solutions become complicated once the effect of rotation is considered. Our numerical algorithm starts with θ_0 and ϕ_0 obtained from Gangadhara (2004) as the initial guess values and finds the refined ones by solving $\hat{n} \cdot \hat{v} = 1$.

The magnetic colatitude θ_0 and azimuth ϕ_0 as functions of rotation phase ϕ'_m are plotted in Figure 2 for both non-rotating (dotted curves) and rotating (solid curves) cases using the parameters $\alpha = 30^\circ$, $P = 1$ s, $r_n = r/r_{\rm LC} = 0.05$, and $\sigma = \pm 5^\circ$. In the rotating case both the minimum of θ_0 and the inflection point of ϕ_0 shift to the earlier rotation phase compared with those in the non-rotating case. The absolute phase shifts of both the θ_0 minimum and the inflection point of ϕ_0 from the fiducial phase ($\phi'_m = 0$) are found to be $2\overset{\circ}{.}9$, which is about $\sim r_n$, as predicted by BCW (1991). For comparison, we superpose the curves (dashed line) due to the BCW (1991) model and find that their approximate analytical solutions are valid only over a smaller rotation phase around $2\overset{\circ}{.}9$.

Even though the observer receives maximum radiation from the emission point (θ_0, ϕ_0) at which $\hat{v}$ and $\hat{n}$ are exactly aligned, the observer also receives considerable radiation from the neighboring emission points due to the finite width of the emission beam. This is about $\sim 2/\gamma$, and the boundary of the emission region centered on $\hat{n}$ is specified by the condition $\hat{n} \cdot \hat{v} = \cos(1/\gamma)$. For computational purposes we discretized the beaming region into "beaming region points" (BRP); the coordinates θ and ϕ of each point are specified by θ_e and ϕ_e, respectively. Since the coordinates θ and ϕ are orthogonal, their ranges $\theta_{e,\rm min} \leqslant \theta \leqslant \theta_{e,\rm max}$ and $\phi_{e,\rm min} \leqslant \phi \leqslant \phi_{e,\rm max}$ can be used to specify the beaming region boundary, where the subscripts (e,min) and (e,max) denote the lower and upper boundaries of the emission region. By considering $\theta_0 - 1/\gamma$ and $\theta_0 + 1/\gamma$ as initial guess values for $\theta_{e,\rm min}$ and $\theta_{e,\rm max}$ at $\phi = \phi_0$, we solve $\hat{n} \cdot \hat{v} = \cos(1/\gamma)$ numerically and find the roots $\theta_{e,\rm min}$ and $\theta_{e,\rm max}$. Next, for any $\theta = \theta_e$ within the range between $\theta_{e,\rm min}$ and $\theta_{e,\rm max}$, we consider $\phi_0 - 1/\gamma$ and $\phi_0 + 1/\gamma$ as the initial guess values for $\phi_{e,\rm min}$ and $\phi_{e,\rm max}$ and again solve $\hat{n} \cdot \hat{v} = \cos(1/\gamma)$ numerically to find the roots $\phi_{e,\rm min}$ and $\phi_{e,\rm max}$. Note that beaming regions on the leading side become broader compared to those on the corresponding trailing side, but they are symmetric in the non-rotating case (Gangadhara 2010). This is because the source trajectories on the leading side get squeezed, whereas on the trailing side they get stretched (e.g., Thomas & Gangadhara 2007).

Note that Equation (4) shows the integration of the electric field of radiation emitted by the relativistic source along its trajectory. The observer receives the beamed radiation only for a small segment of the source trajectory between the points P_i and P_f along a rotating field line (see Figure 1). As the source moves from P_i to P_f along the rotating field line, time changes from t_i to t_f, colatitude θ changes from θ_i to θ_f, and the rotation phase ϕ' of the magnetic axis changes from ϕ'_i to ϕ'_f. From the relation $ds = |\mathbf{b}| d\theta = \kappa c dt$, we deduce the expression for time t:

$$t = \int \frac{|\mathbf{b}|}{\kappa c} d\theta + K, \tag{5}$$

where K is the integration constant. Using the condition $t = \phi'_m/\Omega$ for all $\theta = \theta_e$ within the beaming region, it follows from Equation (5) that $K = (\phi'_m/\Omega) - (\int |\mathbf{b}|/(\kappa c) d\theta)_{\theta=\theta_e}$. Therefore, we have

$$t = \frac{\phi'_m}{\Omega} + \int \frac{|\mathbf{b}|}{\kappa c} d\theta - \left(\int \frac{|\mathbf{b}|}{\kappa c} d\theta \right)_{\theta=\theta_e} \tag{6}$$

and the corresponding $\phi' = \Omega t$ for the source motion along any given field line within the beaming region. Hence, the argument

of the integrand in Equation (4) becomes the function of θ only:

$$\mathbf{E}(\mathbf{r},\omega) = \frac{1}{\sqrt{2\pi}}\frac{qe^{i\omega R_0/c}}{R_0 c} \times \int_{-\infty}^{+\infty} \frac{|\mathbf{b}|}{\kappa c}\frac{\hat{n}\times[(\hat{n}-\boldsymbol{\beta})\times\dot{\boldsymbol{\beta}}]}{\xi^2} e^{i\omega\{t-\hat{n}\cdot\mathbf{r}/c\}}d\theta, \quad (7)$$

where time t has to be replaced by the expression given in Equation (6).

Let

$$\mathbf{A} = \{A_i\} = \frac{|\mathbf{b}|}{\kappa c}\frac{\hat{n}\times[(\hat{n}-\boldsymbol{\beta})\times\dot{\boldsymbol{\beta}}]}{\xi^2}, \quad (8)$$

where A_i with $i = x$, y, and z are the components of $\mathbf{A}$ in the X-, Y-, and Z-directions, respectively (see Figure 1). We series expand the components of $\mathbf{A}$ in powers of θ about θ_e and obtain

$$A_i(\theta) = a_{i0} + a_{i1}(\theta-\theta_e) + a_{i2}(\theta-\theta_e)^2 + O[(\theta-\theta_e)^3], \quad (9)$$

where a_{ij} with $i = x$, y, and z and $j = 0$, 1, and 2 are the series expansion coefficients. They are given by

$$a_{i0} = A_i(\theta_e), \quad a_{i1} = A_i'(\theta_e), \quad a_{i2} = \frac{1}{2}A_i''(\theta_e), \quad (10)$$

where A_i' and A_i'' are the respective first and second derivatives of A_i with respect to θ evaluated at θ_e. Since the expressions of a_{i0}, a_{i1}, and a_{i2} are too big, we have not reproduced them here. However, one can reproduce them by differentiating $\mathbf{A}$.

We set the argument of the exponential in Equation (7), $\omega\{t-\hat{n}\cdot\mathbf{r}/c\} = C$, and series expand in powers of θ about θ_e, to obtain

$$C(\theta) = c_0 + c_1(\theta-\theta_e) + c_2(\theta-\theta_e)^2 + c_3(\theta-\theta_e)^3 + O[(\theta-\theta_e)^4], \quad (11)$$

where c_k with $k = 0, 1, 2$, and 3 are the series expansion coefficients. They are given by

$$c_0 = C(\theta_e), \quad c_1 = C'(\theta_e), \quad c_2 = \frac{1}{2}C''(\theta_e), \quad c_3 = \frac{1}{6}C'''(\theta_e), \quad (12)$$

where C', C'', and C''' are the respective first, second, and third derivatives of C with respect to θ evaluated at θ_e. Since the expressions of c_0, c_1, c_2, and c_3 are too big, we have not reproduced them here.

By substituting Equations (9) and (11) into Equation (7), we obtain the components of $\mathbf{E}(\omega)$:

$$E_i(\omega) = E_0\int_{-\infty}^{+\infty}(a_{i0}+a_{i1}\vartheta+a_{i2}\vartheta^2)e^{i(c_1\vartheta+c_2\vartheta^2+c_3\vartheta^3)}d\vartheta, \quad (13)$$

where $i = x$, y, and z. Here, $\vartheta = \theta - \theta_e$ and $E_0 = qe^{i[(\omega R_0/c)+c_0]}/(\sqrt{2\pi}R_0 c)$.

Next, by substituting the integral solutions S_0, S_1, and S_2 given in the Appendix, we obtain

$$E_i(\omega) = E_0(a_{i0}S_0 + a_{i1}S_1 + a_{i2}S_2). \quad (14)$$

The Stokes parameters I, Q, U, and V have been used as tools to specify the polarization state of the radiation field. The net radiation that the observer tends to receive at any rotation phase ϕ_m' will be an incoherent addition of radiation from bunches from all those emission points which lie within the beaming region. Following the definitions given by Gangadhara (2010), we estimate the resultant Stokes parameters I_s, Q_s, U_s, and V_s.

3. SIMULATION OF PULSE PROFILES

3.1. Emission From the Beaming Region

By assuming uniform source distribution and using the viewing parameters $\alpha = 45^\circ$, $\sigma = 2^\circ$, pulsar rotation period $P = 1$ s, phase $\phi_m' = 0^\circ$, normalized emission height $r_n = 0.01$, particle's Lorentz factor $\gamma = 400$, and observation frequency $\nu = 600$ MHz, we compute the Stokes parameters for the radiation field. The contour plots of I, L, and V in the (θ, ϕ)-plane are given in Figure 3. For comparison we present both non-rotating—panels (a), (b), and (c) and the rotating—panels (a′), (b′), and (c′)—cases. The parameters I, L, and V are normalized with the corresponding maximum value of I within the beaming region. We find that the ratio of peak intensity in the rotating case to that in the non-rotating case is about 2. In all panels, the contour levels are marked on the respective contours. The contours are colored gray in such a way that the darker the region, the lower the corresponding parameter value.

In the non-rotating case, the trajectory of the sources is the same as that of their associated dipolar field lines. Hence, the contours of I and L are symmetric, while those of V are antisymmetric with respect to the (θ, ϕ_0)-plane. In the rotating case, the contours of I, L, and V get rotated in the (θ, ϕ)-plane due to non-uniform aberration within BRP.

Using the parameters $\alpha = 30^\circ$, $\sigma = 5^\circ$, $r_n = 0.05$, $P = 1$ s, $\gamma = 400$, and $\nu = 600$ MHz at discrete rotation phases of the magnetic axis $\phi_m' = -10^\circ$, 0°, and 10°, we simulate the emissions from the beaming region and present the contours of V in Figure 4. In each panel, V is normalized with the corresponding peak intensity $I_{\rm peak}$ within the beaming region. The rotation of the circular contour pattern is more toward the inner rotation phases ($\phi_m' = 0^\circ$) compared to that on the outer rotation phases ($\phi_m' = \pm 10^\circ$). This is because the perpendicular distance from the pulsar spin axis to the beaming region decreases toward the outer rotation phases, hence the smaller rotation effects. Further, the circular contour pattern on the trailing side ($\phi_m' = 10^\circ$) becomes more rotated compared to that on the leading side ($\phi_m' = -10^\circ$). This is due to greater asymmetry in the intrinsic curvature of the field lines between the smaller and larger θ parts within the beaming region on the trailing side compared to that on the leading side.

To describe the behaviors of circular polarization and the swing of PPA, we define the symbols "+/−" for transition of V_s from left-handed (LH) to right-handed (RH) and "−/+" for transition from RH to LH. We call the counterclockwise swing of PPA ($d\psi_s/d\phi_m' > 0$) "ccw" and the clockwise swing ($d\psi_s/d\phi_m' < 0$) "cw."

3.2. Emission with Uniform Source Distribution

Assuming uniform source distribution and using the viewing parameters $\alpha = 30^\circ$, $\sigma = \pm 5^\circ$, $P = 1$ s, $r_n = 0.05$, $\gamma = 400$, and $\nu = 600$ MHz, we compute the Stokes parameters for the curvature radiation. The profiles of I_s, L_s, V_s, and ψ_s are plotted in Figure 5. The parameters in each panel are normalized with the corresponding maximum value of I_s. In both cases of σ, I_s becomes stronger on the leading side ($\phi_m' < 0^\circ$) of the fiducial phase ($\phi_m' = 0^\circ$) than on the trailing side. This is because, due to the rotation-induced curvature, the source trajectories on the leading side become more curved than those on the trailing side. The dip in the intensity near $\phi_m' = 0^\circ$ is due to the larger radius of curvature ρ compared to the other regions. The behavior of L_s is similar to that of I_s except for its smaller values due to the incoherent addition of radiation from bunches. We observe that

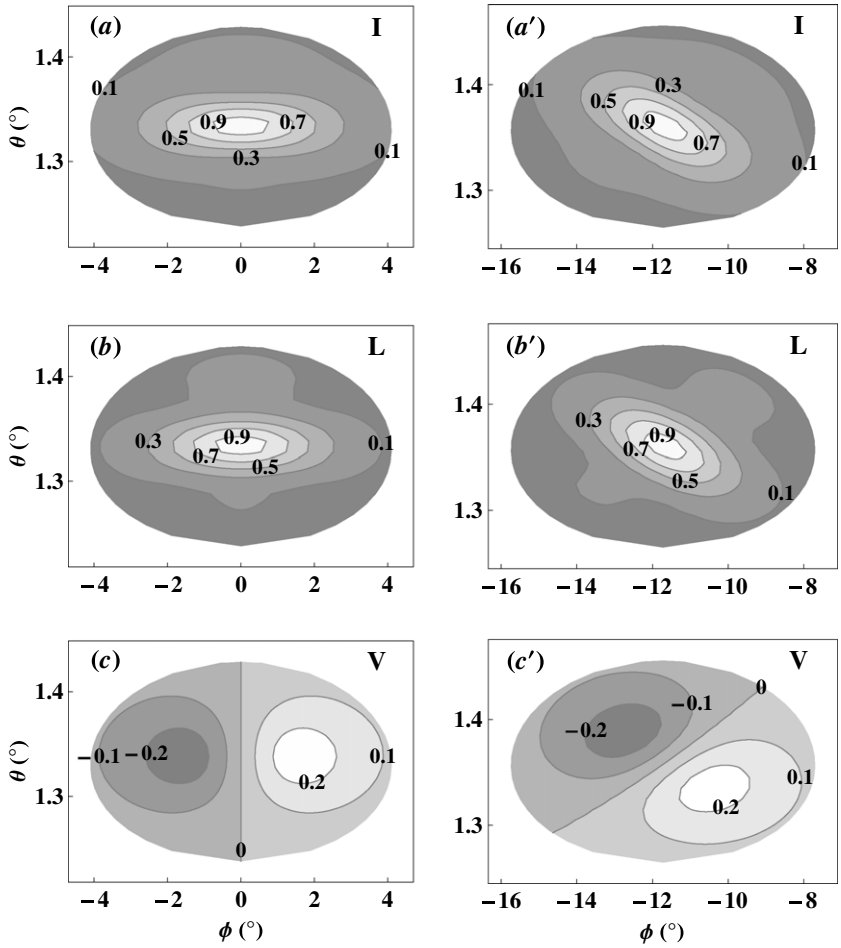

Figure 3. Simulation showing the emission from a beaming region due to an uniform distribution of sources in the non-rotating (left column panels) and rotating (right column panels) cases at $\phi'_m = 0^\circ$. In this simulation, $\alpha = 45^\circ$, $\sigma = 2^\circ$, $r_n = 0.01$, $P = 1$ s, $\gamma = 400$, and $\nu = 600$ MHz.

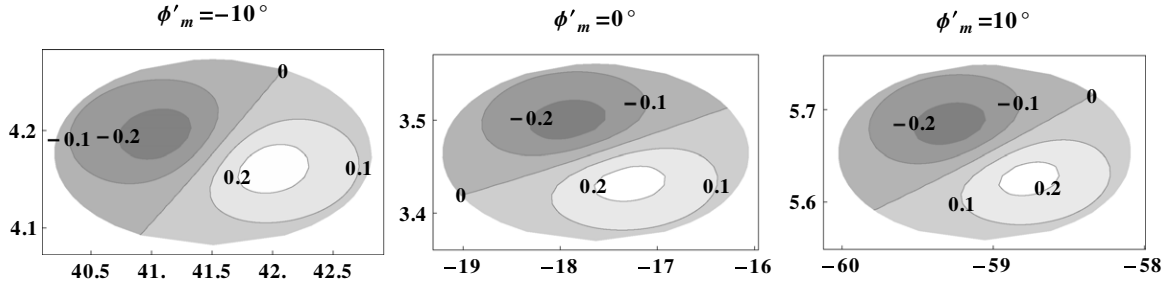

Figure 4. Simulation showing the circular polarization V from the beaming region in the rotating case at three discrete rotation phases. In this simulation, $\alpha = 30^\circ$, $\sigma = 5^\circ$, $r_n = 0.05$, $P = 1$ s, $\gamma = 400$, and $\nu = 600$ MHz.

a small quantity of circular polarization survives due to rotation-induced asymmetry. The PPA is increasing (ccw) in the case of $\sigma = 5^\circ$, whereas it is decreasing (cw) in the case of $\sigma = -5^\circ$. The PPA inflection point, the phase at which $|d\psi_s/d\phi'_m|$ is at its maximum (indicated by an arrow), is found to be shifted to $\phi'_m = 8.^\circ 8$ for $\sigma = 5^\circ$ and to $\phi'_m = 8.^\circ 6$ for $\sigma = -5^\circ$. These shifts are about $3r_n$.

For comparison we have superposed BCW (1991) PPA curves (dotted curves) on our simulated PPA curves. Our simulated PPA profile shapes and the shift of the PPA inflection point are found to be in good agreement with the BCW (1991) model near the central parts ($\phi'_m \sim 0$) but slightly deviated at larger rotation phases due to the approximations made in the BCW (1991) model. Also, note that at any rotation phase ϕ'_m, the BCW (1991) model considers only the emission from the central point of the beaming region, whereas we consider the emissions from the whole of the beaming region.

3.3. Emission with Modulation

In general, pulsar average radio profiles consist of many components, which could be due to emission from plasma columns that are associated with sparks on the polar cap. When sight line cuts through such emissions, it encounters an intensity pattern, which may be treated as approximately Gaussians (e.g., Kramer et al. 1994). We consider time-independent modulation (Gangadhara 2010) so that any fluctuation in the intensity strength of individual pulses will be smoothed out; hence, our simulated profiles are expected to resemble the pulsar average

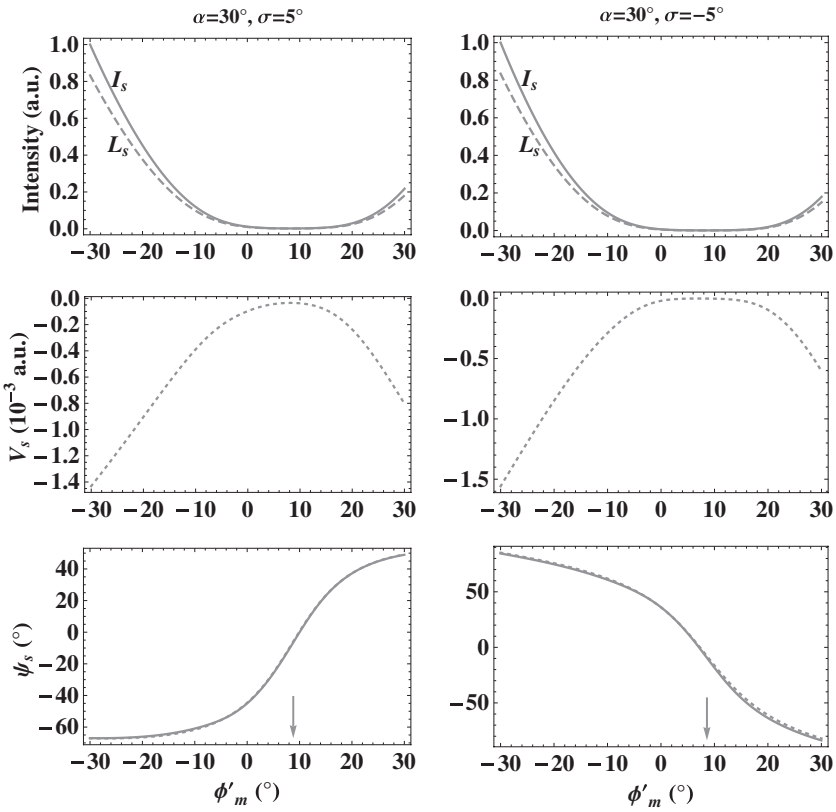

Figure 5. Simulated pulse profiles with $P = 1$ s, $\gamma = 400$, $\nu = 600$ MHz, and $r_n = 0.05$. In the ψ_s panels, solid curves are due to our simulations and the dotted curves are due to BCW (1991) model. The arrows in the ψ_s panels mark the polarization angle inflection points.

profiles. Consider a time-independent Gaussian modulation in both the polar and azimuthal directions:

$$f(\theta, \phi) = \sum f_0 \exp\left[-(\theta - \theta_p)^2/\sigma_\theta^2\right] \exp\left[-(\phi - \phi_p)^2/\sigma_\phi^2\right], \quad (15)$$

where (θ_p, ϕ_p) define the peak location of the Gaussian and f_0 is the amplitude. The parameters $\sigma_\theta = \mathrm{w}_\theta/(2\sqrt{\ln 2})$ and $\sigma_\phi = \mathrm{w}_\phi/(2\sqrt{\ln 2})$, and w_θ and w_ϕ are the corresponding full width at half-maximum (FWHM) of the Gaussian in the two directions. The resultant Stokes parameters I_s, Q_s, U_s, and V_s after taking modulation into account are given in Gangadhara (2010).

3.3.1. Simulation of Core Emission

To explore the effect of rotation on the central core component of pulsar radio profiles, we consider a Gaussian modulation having a peak at $(\theta_p, \phi_p) = (1^\circ, 0^\circ)$. We choose a peak of modulation slightly away from the magnetic axis to have modulation in both the θ- and ϕ-directions. For simulation, we use the viewing parameters $\alpha = 10^\circ$, $\sigma = 2^\circ$, $P = 1$ s, $r_n = 0.02$, $\gamma = 400$, and $\nu = 600$ MHz. Since the minimum of the coordinate θ is $\sim 2/3\sigma = 1.^\circ33$ in this case, the sight line passes through the emission region where modulation strength is slightly below its amplitude. To see the combined effect of rotation and modulation, we consider $\sigma_\phi = 0.15$ and three cases for $\sigma_\theta = 0.15$, 0.004, and 0.002; the simulated polarization profiles are given in Figure 6. In all three cases of σ_θ, intensity profiles are shifted to the earlier phase with respect to the fiducial phase $\phi'_m = 0^\circ$, while the PPA profile shifts to the later phase due to the effect of rotation. Note that in the absence of rotation, the minimum of θ_0 and the antisymmetric point of ϕ_0 (i.e., the phase at which $\phi_0 = 0$) occur at $\phi'_m = 0^\circ$, hence, the intensity will peak at $\phi'_m = 0^\circ$. In the rotating case, intensity peaks shift to earlier phases by about $1.^\circ36$, $1.^\circ31$, and $1.^\circ24$ in the three cases of $\sigma_\theta = 0.15$, 0.004, and 0.002, respectively. The phase shift of the I_s peak is found to decrease with decreasing σ_θ. The reasons are, due to aberration, the minimum of θ_0 and the antisymmetric point of ϕ_0; hence, the peak of modulation (the phase at which the observer encounters maximum modulation strength) shifts to an earlier phase. The emission due to uniform source distribution becomes stronger on the leading side of the modulation peak compared to that on the trailing side. Therefore, the peak of modulated total intensity will be further advanced in phase with respect to the peak of modulation. However, this extra phase shift of modulated intensity peaks with respect to modulation peaks favors the formation of a more symmetric component: larger unmodulated emission on the smaller radius of the curvature side will be less enhanced by weaker modulation, whereas smaller unmodulated emission on the larger radius of the curvature side will be more enhanced by stronger modulation. Note that if the modulation is steeper, the intensity profile closely follows the modulation. Hence, the pulse width and the phase shift of the peak of the total intensity will decrease as we go from $\sigma_\theta = 0.15$ to $\sigma_\theta = 0.002$.

In the case of $\sigma_\theta = 0.15$, the circular polarization is antisymmetric and the transition is from RH (negative) to LH (positive). The leading negative circular is found to be stronger compared to that on the trailing positive circular, whereas they are equal in the non-rotating case (Gangadhara 2010). The asymmetry in the strengths of negative and positive circulars can be explained as follows: due to rotation, the pattern of circular polarization (see Figure 3) gets rotated in the (θ, ϕ)-plane;

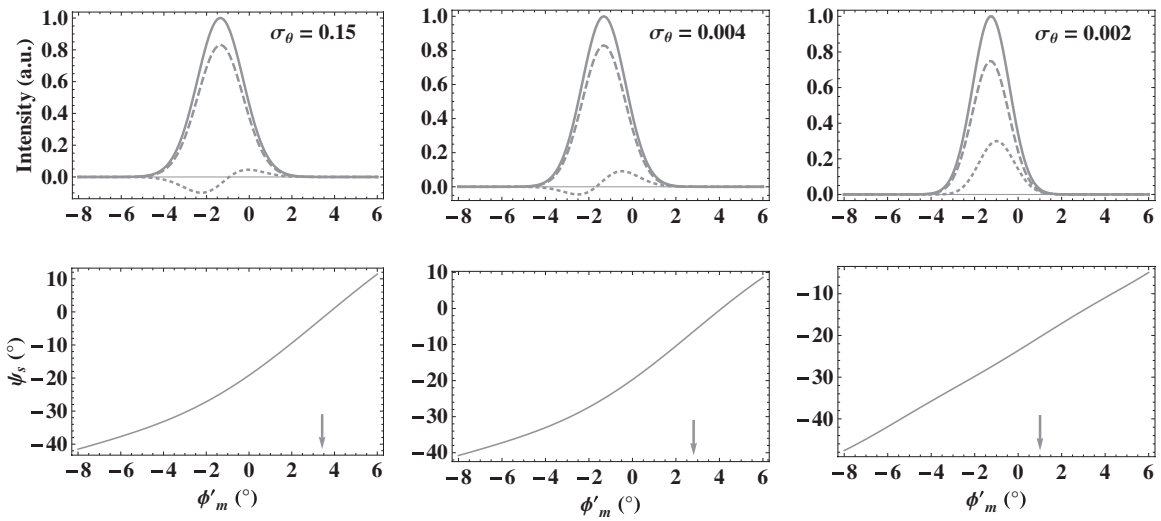

Figure 6. Simulated pulse profiles with $\alpha = 10^\circ$, $\sigma = 2^\circ$, $P = 1$ s, $r_n = 0.02$, $\gamma = 400$, $\nu = 600$ MHz, $f_0 = 1$, $\theta_p = 1^\circ$, $\phi_p = 0^\circ$, and $\sigma_\phi = 0.15$. In each panel I_s (solid curves), L_s (dashed curves), and V_s (dotted curves) are normalized with the respective peak intensity. The arrows in the ψ_s panels mark the polarization angle inflection points.

hence, an asymmetry is introduced in both the θ- and ϕ-directions. Since we used $\theta_p = 1^\circ$ and the minimum of θ that the observer encounters is $\sim 1.^\circ 3$, the modulation in the θ-direction always enhances the emission over smaller values of θ (see Figure 3) compared to that over larger values of θ within the beaming region. Further, since we used $\phi_p = 0^\circ$, modulation in the ϕ-direction selectively enhances the emissions over smaller values of $|\phi|$ compared to those over larger values of $|\phi|$ within the beaming region. Since $\sigma_\phi = \sigma_\theta$ and the beaming regions are more extended in ϕ compared to those in θ, the modulation gradient in ϕ dominates that in θ. Further, the magnitude of rotation of the circular polarization pattern within the beaming region is greater for the inner rotation phases (phases closer to $\phi'_m = 0^\circ$) as compared to that on outer phases (see Figure 4). Hence, modulation can selectively enhance the leading negative circular over the trailing positive circular. Also, because of the above stated reasons, the phase location of the sign reversal of the circular is found to be lagging the phase location of the peak of the total intensity by a small amount.

In the case of $\sigma_\theta = 0.004$, the trailing positive circular becomes stronger than the leading negative circular, which is opposite to $\sigma_\theta = 0.15$. Even though the effect of rotation on the pattern of circular polarization is the same as that in the case of $\sigma_\theta = 0.15$, the modulation becomes comparatively stronger in the θ-direction as $\sigma_\theta \ll \sigma_\phi$. Hence, on the leading side, the net two-dimensional modulation selectively enhances emission over the lower left part of the beaming region, whereas on the trailing side, it selectively enhances the emission over the lower right part (see Figure 4). Hence, the positive circular on the trailing side becomes stronger compared to the negative circular on the leading side. Due to the above stated reasons, the phase of sign reversal of the circular is found to lead the phase of the total intensity peak by a small amount.

In the extreme case of $\sigma_\theta = 0.002$, modulation becomes much stronger in the θ-direction. Therefore, the modulation selectively enhances the emission over the lower part of the beaming region throughout the pulse window. Hence, the circular polarization becomes almost positive throughout the pulse. Again due to asymmetry in the magnitude of the rotation of the circular polarization pattern with respect to rotation phase ϕ'_m, the surviving positive circular is found to be stronger on the trailing side as compared to that on the leading side.

In all three cases, L_s almost follows I_s except for its magnitude. Further, when V_s is weaker, L_s is found to be slightly stronger and vice versa. In all three cases, PPA swing is "ccw" and PPA inflection points (indicated by arrows) are found to be shifted to later phases by $3.^\circ 42$, $2.^\circ 82$, and $1.^\circ 00$, respectively. The phase shift of the position angle inflection point is found to decrease with decreasing σ_θ due to the combined effect of rotation and modulation.

BCW (1991) predicted that due to aberration both the θ minimum and the antisymmetric point of ϕ shift to an earlier phase by $\sim r_n$, ($1.^\circ 14$ for $r_n = 0.02$), with respect to the fiducial phase $\phi'_m = 0^\circ$. They assumed that the centroid of the intensity profile coincides with the θ minimum and the antisymmetric point of ϕ. Further, by using the particle acceleration vector, which reflects the direction of the electric field vector in time domain, BCW (1991) also predicted the shift of the PPA inflection point to a later phase by $\sim 3r_n$, ($3.^\circ 44$ for $r_n = 0.02$). However, in our model, we estimate the radiation field in the frequency domain. We consider the effect of rotation along with modulation and a detailed geometry of emission region, which includes finite beaming regions from which the observer can receive considerable radiation, which is not considered in the BCW (1991) model. Hence, the phase shifts of the total intensity and PPA inflection points can be significantly different from those predicted by BCW (1991).

Note that if one considers the retardation (radiation propagation time delay), the emissions from the beaming region at any rotation phase ϕ'_m will arrive at a later time, i.e., by delay $\delta t = \hat{n} \cdot \mathbf{r}/c$; hence, the phase is delayed by $\delta\phi'_{\rm ret} = \Omega\delta t$ (e.g., Gangadhara 2005). However, since we have assumed that emissions from the whole beaming region originate from a particular altitude r for a given phase ϕ'_m, they will have roughly the same $\delta t \sim r/c$ (which at most differ by $\sim 10^{-8}$ s between center and boundary within the beaming region). Hence, emissions will arrive at the same time $t_r = t_e + \delta t$, where t_e and t_r are the emission and reception times of the radiation, respectively. Further, since we consider a constant r across the whole pulse, the net emission due to the whole beaming region at any phase ϕ'_m will

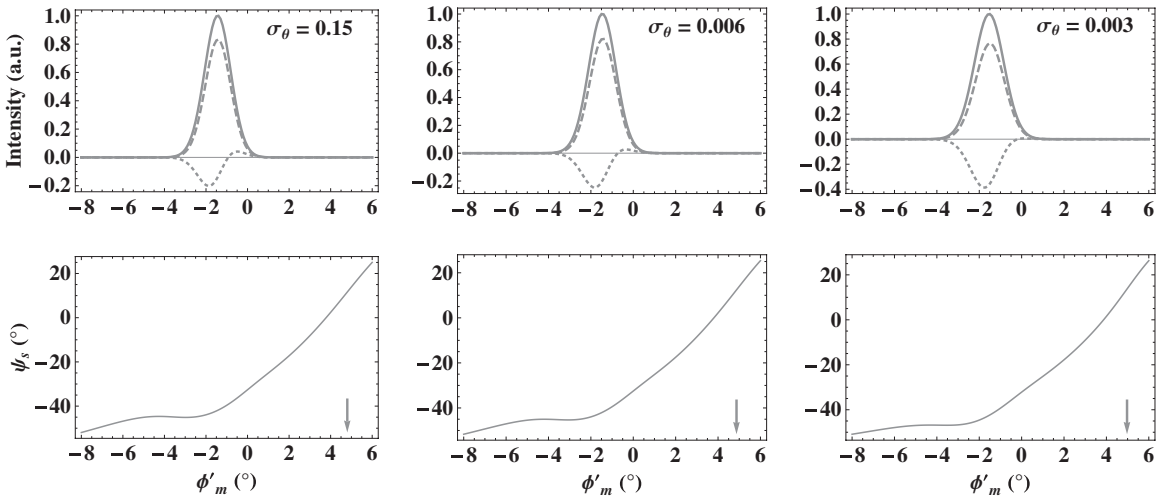

Figure 7. Simulated pulse profiles with $\sigma = 1°$. The other parameters are the same as those in Figure 6.

be time delayed by the same $\delta t \sim r/c$. Hence, a constant phase delay of $\delta\phi'_{\rm ret} \sim \Omega r/c = r/r_{\rm LC} = r_n$ across the whole pulse is introduced. After taking into account retardation along with aberration, the phase shifts of the intensity peak and PPA inflection point in the case $\sigma_\theta = 0.15$ of Figure 6, for example, will be 2.°50 and 2.°28, respectively. Since retardation just causes the shift of the entire aberrated profile by $\delta\phi'_{\rm ret}$ to the earlier phase, we have not reproduced simulations combining retardation and aberration. However, the shapes of the aberrated profile will be affected if one considers the varying altitude across the pulse.

Also note that if one considers modulation that is broader than that considered in the case of $\sigma_\phi = \sigma_\theta = 0.15$ of Figure 6, then the aberration phase shift of the intensity peak becomes substantially different from r_n. Further, V_s becomes almost symmetric with negative circular throughout the profile. This is because as modulation becomes broader, the pulse also becomes broader. Further in Figure 6, we keep σ_ϕ constant and varied σ_θ for the three cases. On the other hand, if one considers the case in which σ_θ is kept constant and σ_ϕ varies from a broader modulation to a steeper one, then the behavior of the total intensity and PPA profiles will be similar to Figure 6. But the evolution of V_s will be from an almost symmetric type to an antisymmetric type due to the above-mentioned reasons. Also, if one considers the case in which both σ_ϕ and σ_θ vary by the same amount from a broader modulation to a steeper one, then the behavior of pulse profiles will be similar to the case in which σ_θ is kept constant and σ_ϕ varies from larger to smaller values. Further, if one considers the negative σ then the polarization profiles behave similarly to the positive σ except for the fact that the polarities of V_s and swing of PPA profile will be opposite.

To see the combined effect of rotation and modulation in the case of the sight line passing through the other side of the emission region, which lies toward the magnetic axis, we consider a sight line with $\sigma = 1°$. For simulations we keep the other parameters the same as those of the $\sigma = 2°$ case in Figure 6. The simulated polarization profiles for $\sigma_\phi = 0.15$ and the three cases $\sigma_\theta = 0.15$, 0.006, and 0.003 are given in Figure 7. The phase shifts of the total intensity peak in the cases $\sigma_\theta = 0.15$, 0.006, and 0.003 are found to be 1.°44, 1.°46, and 1.°53, respectively. The phase shift of the intensity peak tends to increase with decreasing σ_θ, a behavior opposite to the case of $\sigma = 2°$ (see Figure 6). This is because, since we have chosen $\theta_p = 1°$, the emission point coordinate θ will be closer to θ_p at the outer rotation phases $|\phi'_m| > 0°$. The minimum of the emission point coordinate $|\phi|$ will be closer to the chosen $\phi_p = 0°$ for the inner earlier rotation phases. Therefore, the modulation mapped onto a broader pulse phase as σ_θ decreases. Hence, the phase shift of the intensity peak increases as we go from $\sigma_\theta = 0.15$ to 0.003.

In the case of $\sigma_\theta = 0.15$, circular polarization is marginally antisymmetric and the transition is from negative to positive. The leading negative circular is found to be much stronger than the trailing positive circular compared to $\sigma_\theta = 0.15$ of Figure 6. Due to viewing geometry, the observer tends to receive radiation from the beaming region whose emission points in θ are always smaller than $\theta_p = 1°$ in this case. Hence, the net modulation selectively enhances emission over the upper left part of the beaming region (see Figure 4) on the leading side, whereas it selectively enhances the emission over the upper right part of the beaming region on the trailing side. Hence, from Figure 4 we see that the leading negative circular becomes much stronger than the trailing positive circular. The phase lag of the location of sign reversal of the circular with respect to the intensity peak is found to be more compared to that in the case of $\sigma = 2°$ and $\sigma_\theta = 0.15$. In the case of $\sigma_\theta = 0.006$, the negative circular becomes even stronger compared to the positive circular, and in the extreme case of $\sigma_\theta = 0.003$, the circular becomes symmetric, i.e., only the negative circular survives throughout the pulse.

In all three cases, the position angle swing is "ccw" and the phase shifts of its inflection point for $\sigma_\theta = 0.15$, 0.006, and 0.003 are found to be 4.°80, 4.°87, and 4.°97, respectively. The phase shift of the position angle inflection point is found to increase with decreasing σ_θ, unlike that in the case of $\sigma = 2°$ where it decreases with decreasing σ_θ. The observed opposite trend in the phase shift of the PPA inflection point with respect to modulation parameter σ_θ is due to the opposite trend in the selective enhancement of the emission over a part of the beaming region in the two cases of σ.

Note that so far we have considered the general cases of core modulation where the modulation peak is located slightly away from the magnetic axis and is modulated in both the θ- and ϕ-coordinates. The more plausible case for core modulation is a Gaussian whose peak is located at the magnetic axis, i.e., at $\theta_p = 0°$, and depends only in θ. The corresponding modulation function that follows from Equation (15) is $f(\theta) =$

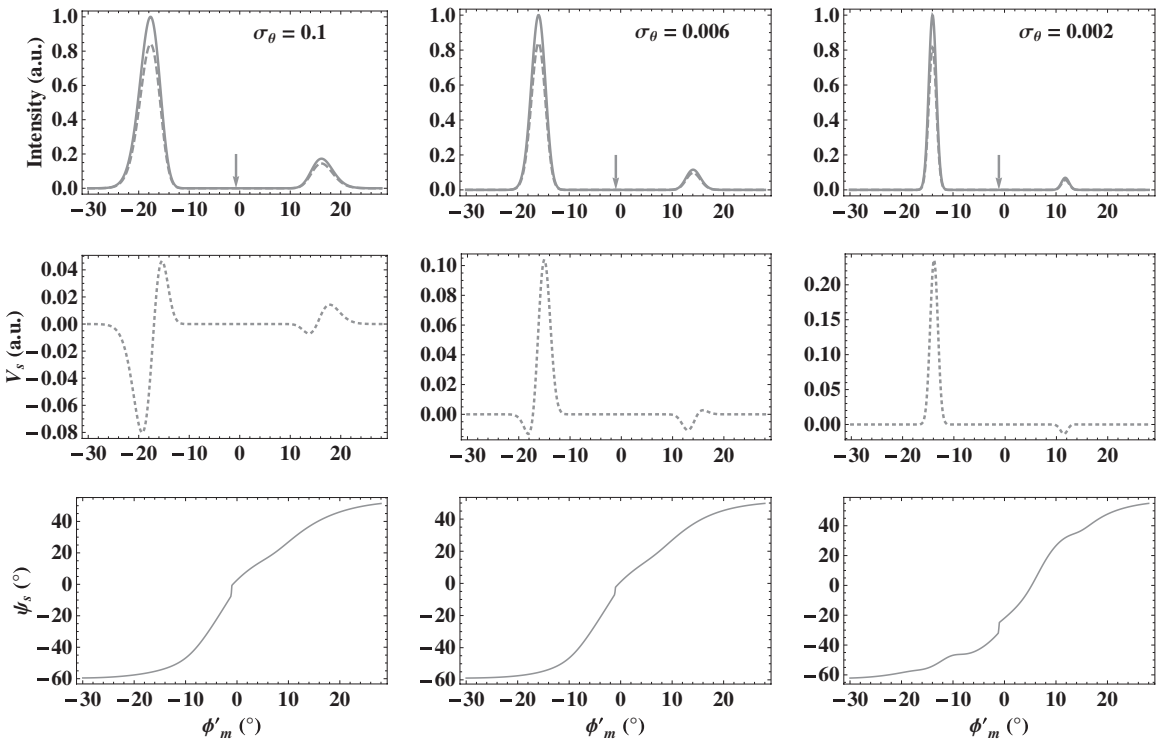

Figure 8. Simulated pulse profiles. The parameters are the same as those in Figure 6 except $(\theta_p,\ \phi_p) = (2^\circ,\ \pm 65^\circ)$ and $\sigma_\phi = 0.1$.

$f_0 \exp(-\theta^2/\sigma_\theta^2)$. If one simulates the pulse profiles with this modulation, V_s becomes a symmetric type: a positive circular (LH) for positive σ and a negative circular (RH) for negative σ throughout the pulse due to the selective enhancement. Note that in the non-rotating model (Gangadhara 2010), the modulation in only the θ-direction will never give the considerable net circular irrespective of its gradient, as it always enhances both the positive and negative circulars by the same amount (see panel (c) in Figure 3).

3.3.2. Simulation of Conal Emission

In this section, we consider the combined effect of rotation and modulation on the concentric conal emissions. Consider two Gaussians whose peaks are situated at $(\theta_p, \phi_p) = (2^\circ, \pm 65^\circ)$ and for which the rest of the parameters are the same as those in Figure 6. The modulation peak locations are chosen such that the sight line passes through the emission regions with modulation strengths below its amplitude and the region of maximum modulation encountered by the observer lies toward the meridional plane. The simulated polarization profiles are given in Figure 8 for the three cases of $\sigma_\theta = 0.1$, 0.006, and 0.002. In all three cases, the leading side component becomes stronger than the trailing side component. This is due to the combined effect of enhancement in the intrinsic unmodulated emission and the modulation strength on the leading side over the trailing side. However, the enhancement due to unmodulated emission is more prominent. In the IOF, due to aberration, the plasma bunch trajectories become more curved on the leading side compared to those on the trailing side; hence, more emission occurs on the leading side. The marginal decrease in the strength of the trailing side component as we go from the case $\sigma_\theta = 0.1$ to 0.002 is due to weaker modulation encountered in the sight line on the trailing side. Further, in all cases of σ_θ, the trailing side component becomes considerably narrower than the leading side component. This is because even though the modulation has roughly the same steepness on both the leading and trailing sides, the radius of curvature becomes steeper in the phase on the trailing side compared to that on the leading side. Hence, it results in a broader component on the leading side. The phase shifts of the mid-point of intensity peaks (the cone centers indicated by arrows) to the earlier phase in the cases $\sigma_\theta = 0.1$, 0.006, and 0.002 are found to be $0\overset{\circ}{.}74$, $0\overset{\circ}{.}94$, and $1\overset{\circ}{.}10$, respectively.

In the case of $\sigma_\theta = 0.1$, the negative circular becomes stronger compared to the positive circular on the leading side and vice versa on the trailing side. This is because the magnitude of rotation of the circular pattern is greater for inner rotation phases, while the net modulated emission is slightly smaller compared to outer phases, hence, the selective enhancement of outer side circulars within the intensity components. In the case of $\sigma_\theta = 0.006$, the positive circular became stronger compared to the negative circular over the leading side component and vice versa over the trailing side component. In the case of $\sigma_\theta = 0.1$, the modulation is broader, hence, the sight line encounters both parts of modulation that are lying toward and away from the meridional plane. As σ_θ decreases, the observer tends to selectively encounter the parts of modulation that are closer to the meridional plane. This selectively enhances the V_s which lies toward $\phi_m = 0^\circ$. Hence, the inner sides of V_s become stronger as compared to the outer sides over both the leading and trailing sides of I_s. In the extreme case of $\sigma_\theta = 0.002$, V_s becomes a symmetric type, i.e., positive on the leading side and negative on the trailing side.

In all cases of σ_θ the linear polarization L_s profile almost follows the total intensity I_s, and PPA swing is "ccw." The distortions or kinks are due to the combined effect of rotation and modulation on the emissions over the beaming regions. The phase shift of the PPA inflection point has become uncertain, as the kinks affect the central part of the position

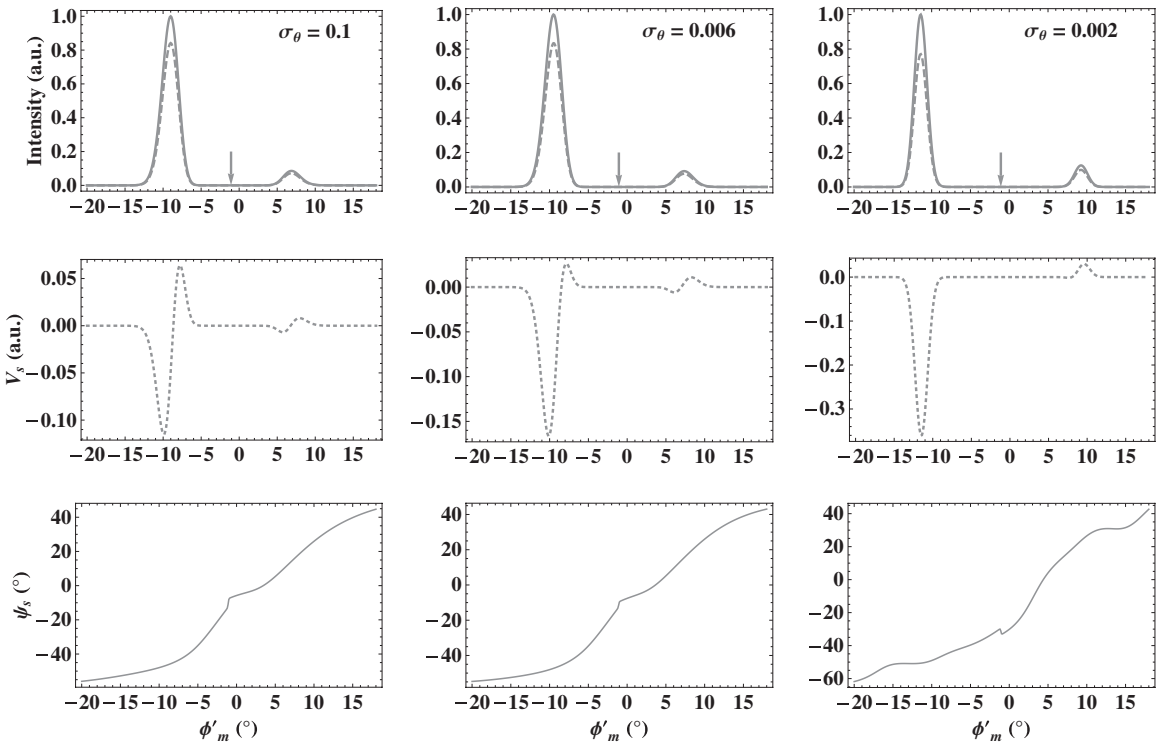

Figure 9. Simulated pulse profiles. The parameters are the same as those in Figure 8 except $\phi_p = \pm 40^\circ$.

angle curves. However, if one considers a case in which the central core component lies between two conal components, then the position angle inflection point can be found without difficulty.

For the next case, we select modulations with peaks at different azimuthal locations ($\phi_p = \pm 40^\circ$) on the same conal ring considered in Figure 8. In this case, the sight line passes through the emission regions with modulation strengths below its amplitude, and the region of maximum modulation encountered by the observer lies away from the meridional plane. By keeping other viewing parameters the same as those in the case of Figure 8, we simulate the polarization profiles for the cases of $\sigma_\theta = 0.1$, 0.006, and 0.002, given in Figure 9. The small increase in the strength of the trailing side component as we go from $\sigma_\theta = 0.1$ to 0.002 is due to an increase in the modulation strength that the observer encounters on the trailing side. The phase shift of the cone centers to the earlier phase in the cases $\sigma_\theta = 0.1$, 0.006, and 0.002 are found to be 1.°07, 1.°06, and 1.°08, respectively. These shifts are found to be almost independent of σ_θ unlike in the previous cases in which they are considerably dependent on the σ_θ. In the case of $\sigma_\theta = 0.1$, V_s is antisymmetric on both the leading and trailing sides, with the outer circular being stronger than the inner. This is similar to the case of $\sigma_\theta = 0.1$ in Figure 8, where the modulation is broader. In the case of $\sigma_\theta = 0.006$, V_s is again antisymmetric on both the leading and trailing sides, but the outer circular dominates over the inner. This is because the sight line encounters the major part of the modulation, which lies away from the meridional plane. Hence, there is a selective enhancement of the outer circular relative to the inner. In the extreme case of $\sigma_\theta = 0.002$, V_s becomes symmetric on both the sides: negative on the leading side and vice versa on the trailing. These are the opposite behaviors of those seen in Figure 8. In all three cases of σ_θ, L_s almost follows I_s with lower values similar to the previous cases, and the PPA swing is "ccw" and shows kinky behavior.

4. DISCUSSION

Pulsar rotation along with modulation and viewing geometry seems to greatly influence pulsar radio profiles. Due to rotation the trajectories of sources on the leading side become more curved compared to those on the trailing side; hence, the leading side unmodulated emission always dominates the trailing one. If one considers azimuthally symmetric cone modulations, then the leading side intensity components become stronger than the corresponding trailing ones due to the rotationally induced asymmetry in the curvature of plasma trajectories (e.g., Thomas & Gangadhara 2007). In support of this, there is a strong observational result by Lyne & Manchester (1988); our simulations clearly confirm it. We also find that the leading side intensity components become wider than the corresponding trailing ones due to asymmetry in the gradient of the radius of curvature between the leading and trailing sides. These findings have observational evidence (Ahmadi & Gangadhara 2002), and a similar behavior has been discussed by Dyks et al. (2010). Note that if we consider higher emission altitude in our simulations then the trailing side component gets substantially weaker or even vanishes. Hence, it could serve as an explanation for the "partial cones" (Thomas et al. 2010).

The facts of the phase shift of the intensity components to earlier rotation phases and that of the PPA inflection point to a later phase are a natural consequence of the effect of rotation. The phase shifts of the centroid of pulse and that of the PPA inflection points have been predicted to be about r_n and $3r_n$, respectively (BCW 1991). Their simplistic model considered only the emission from the points at which the source velocity vector exactly aligns with the observer's sight line. However, there is considerable emission from the other points of the beaming region, which is influenced by rotation and modulation. As a result the shifts of the intensity component and the PPA inflection point will no longer remain as r_n and $3r_n$, respectively.

We have shown that, due to pulsar corotation, the pattern of emission within the beaming region gets rotated in the (θ, ϕ)-plane; hence, an asymmetry is introduced in both the θ- and ϕ-directions. Due to these asymmetries within the beaming region, either antisymmetric- or symmetric-type circular polarization becomes possible depending upon the viewing geometry and modulation. If the modulation is steeper and has roughly the same gradient in both θ and ϕ, then antisymmetric circular polarization is observed. On the other hand, symmetric-type circular polarization is more plausible when modulation is broader and has roughly the same gradient in both θ and ϕ, and also when modulation is steeper in θ than in ϕ. In the literature, circular polarization has been modeled only in the non-rotating pulsar approximation. Hence, only the antisymmetric circular polarization was thought to be a natural feature of curvature radiation, and the symmetric-type circular polarization was speculated to be a consequence of the propagation effect (e.g., Gil et al. 1993; Gangadhara 2010).

Han et al. (1998) and You & Han (2006) found that the sign reversal of circular polarization is not only associated with the central "core" region but is also found over conal components as well as at the intersection of conal components. From our simulations of conal components, it is possible to explain all types of circular polarization sense reversals and their association with either increasing or decreasing PPA seen in Table 3 in You & Han (2006). For example, consider Figures 8 and 9 in the case of $\sigma_\theta = 0.1$. On the leading side, we get a case in which the circular polarization changes sign from negative to positive with an increasing PPA. Again by considering the $\sigma_\theta = 0.002$ cases of Figures 8 and 9, on the leading side we can get a case in which circular polarization changes sign from positive to negative with increasing PPA.

We confirm Radhakrishnan & Rankin's (1990) correlation that the sense reversal of circular polarization from negative to positive is correlated with "ccw" PPA swing (or increasing PPA) and vice versa, and we argue that this is a geometric property of curvature radiation. In pulsars with "symmetric"-type circular polarization, Han et al. (1998) did not find any correlation between the sense of circular polarization and the PPA swing. Our simulations also indicate that negative circular polarization can be associated with either "ccw" or "cw" PPA swing depending upon the viewing geometry and modulation locations. Similarly, the positive circular can also be associated with "ccw" or "cw" PPA swing. However, Han et al. (1998) and You & Han (2006) found that many conal–double pulsars show a single-handed circular polarization over both components. The negative circular correlates with the "ccw" PPA swing and the positive circular correlates with the "cw" PPA swing.

Our simulations of conal components show that if the sight line is missing the modulation peaks and the steepness of modulation in the polar (θ) direction is much larger as compared to that in the azimuthal (ϕ) direction, then the circular polarization becomes single handed on both the leading and trailing sides, but with opposite signs (see, for example, case $\sigma_\theta = 0.002$ of Figures 8 and 9). Note that we consider situations in which the leading and trailing side modulations symmetrically lie on a cone centered on the magnetic axis. On the other hand, if one considers a situation in which the modulations are asymmetrically located on a cone, then the correlation between the sense of circular polarization and the PPA swing in the case of conal–double pulsars can be explained. For example, by choosing the locations of modulations in the case of $\sigma_\theta = 0.002$ of Figure 9 as $\phi_p = 40^\circ$ and -65°, one can get negative circulars over both the leading and trailing components (see the cases $\sigma_\theta = 0.002$ of Figures 8 and 9); hence, an association of negative circular with the increasing PPA can be established.

The "kinky"-type distortion in the PPA profile has been found in some normal pulsars and more commonly in millisecond pulsars. Mitra et al. (2000) attributed this effect to a multipolar magnetic field, while Mitra & Seiradakis (2004) speculated that the aberration/retardation resulting from the height-dependent emission can cause the distorted PPA traverses. Ramachandran & Kramer (2003), following Hibschman & Arons (2001), proposed that the discrete jumps in the PPA profiles are due to magnetospheric return currents. However, from our simulations it is clear that even with a constant emission altitude across the whole pulse profile, "kinky" behaviors can be produced in PPA traverses. Due to an incoherent addition of radiation field emitted from a beaming region, which is affected by rotation and modulation, the distortions in the PPA traverses are introduced. The PPA traverses under both the core and conal components are found to become distorted. There are, however, observational claims that central core region is more likely than the conal regions to show RVM distortions (e.g., Rankin 1983, 1990; Radhakrishnan & Rankin 1990).

In this work we consider a constant emission altitude r across the whole pulse to make comparison with the earlier results. However, varying emission altitude across the pulse can be incorporated. We consider only the rotation and time-independent modulation effects in our simulations, as we are interested in the polarization properties of curvature radiation that is of intrinsic origin. We plan to consider the propagation effects, polar cap currents, magnetic field sweep back, and higher multipolar components of the magnetic field on pulsar radio emission in our future works.

5. CONCLUSION

By developing a relativistic model for pulsar radio emission, we have attempted to explain the complete polarization state of the curvature radiation. Our model takes into account, as detailed in Section 3.3, a very detailed geometry of emission region, rotation, and modulation which has not been much incorporated in the earlier models. Based on our pulse profile simulations, we conclude the following.

1. The phase shift of intensity components to an earlier phase and the PPA inflection point to a later phase are strongly influenced by the combined effect of rotation and modulation.
2. The components on the leading side become stronger and broader than those on the trailing side because of rotation.
3. In an unmodulated emission, a small quantity of circular polarization survives due to rotationally induced asymmetry, but from the point of view of observations it is insignificant at lower altitudes $r_n < 0.05$.
4. For the very first time we are able to show that "symmetric"-type circular polarization can be obtained within the framework of curvature radiation. This result is very important from the point of view of the emission mechanism.
5. Both types of circular polarization, antisymmetric (+/− or −/+) and symmetric (+ or −), can result anywhere within the pulse window due to the combined effect of

rotation, viewing geometry, and modulation. This might be responsible for the diverse nature of circular polarization.
6. We argue that pulsar rotation combined with modulation can introduce "kinky" patterns into the PPA traverses.

We thank J. L. Han and Pengfei Wang for stimulating discussions and the anonymous referee for useful comments.

APPENDIX

Consider the integral

$$S_0 = \int_{-\infty}^{+\infty} e^{i(c_1\vartheta + c_2\vartheta^2 + c_3\vartheta^3)} d\vartheta. \quad \text{(A1)}$$

By changing the variable of integration $\vartheta = (x/l) + m$ and defining the constants $l = \sqrt[3]{3c_3}$ and $m = -c_2/(3c_3)$, we obtain

$$\int_{-\infty}^{+\infty} e^{i(c_1\vartheta + c_2\vartheta^2 + c_3\vartheta^3)} d\vartheta = U \int_{-\infty}^{+\infty} e^{i\left(zx + \frac{x^3}{3}\right)} dx, \quad \text{(A2)}$$

where $z = \frac{1}{\sqrt[3]{3c_3}}\left(c_1 - \frac{c_2^2}{3c_3}\right)$ and $U = \frac{1}{\sqrt[3]{3c_3}} e^{i\frac{c_2}{3c_3}\left(\frac{2c_2^2}{9c_3} - c_1\right)}$.

For $\mathrm{Im}(z) = 0$, we know

$$j_0 = \int_{-\infty}^{\infty} \mathrm{e}^{i\left(zx + \frac{x^3}{3}\right)} dx = 2\pi\, Ai(z), \quad \text{(A3)}$$

where $\mathrm{Ai}(z)$ is an entire Airy function of z with no branch cut discontinuities, and

$$j_1 = \int_{-\infty}^{\infty} x e^{i\left(zx + \frac{x^3}{3}\right)} dx = -i2\pi\, Ai'(z), \quad \text{(A4)}$$

where $Ai'(z)$ is the derivative of the Airy function $Ai(z)$. Therefore, we have

$$S_0 = U j_0. \quad \text{(A5)}$$

By differentiating Equation (A2) with respect to c_1, we obtain

$$\begin{aligned} S_1 &= \int_{-\infty}^{+\infty} \vartheta\, e^{i(c_1\vartheta + c_2\vartheta^2 + c_3\vartheta^3)} d\vartheta \\ &= \frac{U}{\sqrt[3]{3c_3}} \int_{-\infty}^{+\infty} \left(x - \frac{c_2}{\sqrt[3]{3c_3^2}}\right) e^{i\left(z\,x + \frac{x^3}{3}\right)} dx \\ &= \frac{U}{\sqrt[3]{3c_3}} \left(j_1 - \frac{c_2}{\sqrt[3]{9c_3^2}} j_0\right). \end{aligned} \quad \text{(A6)}$$

Differentiation of Equation (A2) with respect to c_2 gives

$$\begin{aligned} S_2 &= \int_{-\infty}^{+\infty} \vartheta^2 e^{i(c_1\vartheta + c_2\vartheta^2 + c_3\vartheta^3)} d\vartheta \\ &= \frac{U}{3c_3} \int_{-\infty}^{+\infty} \left(\frac{2c_2^2}{3c_3} - c_1 - \frac{2c_2}{\sqrt[3]{3c_3}} x\right) e^{i\left(zx + \frac{x^3}{3}\right)} dx \\ &= \frac{U}{3c_3} \left[\left(\frac{2c_2^2}{3c_3} - c_1\right) j_0 - \frac{2c_2}{\sqrt[3]{3c_3}} j_1\right]. \end{aligned} \quad \text{(A7)}$$

REFERENCES

Ahmadi, P., & Gangadhara, R. T. 2002, ApJ, 566, 365
Blaskiewicz, M., Cordes, J. M., & Wasserman, I. 1991, ApJ, 370, 643
Cheng, A. F., & Ruderman, M. A. 1979, ApJ, 229, 348
Cheng, A. F., & Ruderman, M. A. 1980, ApJ, 235, 576
Dyks, J. 2008, MNRAS, 391, 859
Dyks, J., Rudak, B., & Harding, A. K. 2004, ApJ, 607, 939
Dyks, J., Wright, G. A. E., & Demorest, P. 2010, MNRAS, 405, 509
Gangadhara, R. T. 1997, A&A, 327, 155
Gangadhara, R. T. 2004, ApJ, 609, 335
Gangadhara, R. T. 2005, ApJ, 628, 923
Gangadhara, R. T. 2010, ApJ, 710, 29
Gangadhara, R. T., & Gupta, Y. 2001, ApJ, 555, 31
Gil, J. A., Kijak, J., & Zycki, P. 1993, A&A, 272, 207
Gil, J. A., & Snakowski, J. K. 1990a, A&A, 234, 237
Gil, J. A., & Snakowski, J. K. 1990b, A&A, 234, 269
Gupta, Y., & Gangadhara, R. T. 2003, ApJ, 584, 418
Han, J. L., Manchester, R. N., Xu, R. X., & Qiao, G. J. 1998, MNRAS, 300, 373
Hibschman, J. A., & Arons, J. 2001, ApJ, 546, 382
Kazbegi, A. Z., Machabeli, G. Z., & Melikidze, G. J. 1991, MNRAS, 253, 377
Komesaroff, M. M. 1970, Nature, 225, 612
Kramer, M., Wielebinski, R., Jessner, A., Gil, J. A., & Seiradakis, J. H. 1994, A&AS, 107, 515
Krzeszowski, K., Mitra, D., Gupta, Y., et al. 2009, MNRAS, 393, 1617
Lyne, A. G., & Manchester, R. N. 1988, MNRAS, 234, 477
Lyubarskii, Y. E., & Petrova, S. A. 1999, Ap&SS, 262, 379
Melrose, D. B. 2003, in ASP Conf. Ser. 302, Radio Pulsars, ed. M. Bailes, D. J. Nice, & S. E. Thorsett (San Francisco, CA: ASP), 179
Michel, F. C. 1987, ApJ, 322, 822
Mitra, D., & Deshpande, A. A. 1999, A&A, 346, 906
Mitra, D., Konar, S., Bhattacharya, D., et al. 2000, in ASP Conf. Ser. 202, IAU Colloq. 177: Pulsar Astronomy—2000 and Beyond, ed. M. Kramer, N. Wex, & N. Wielebinski (San Francisco, CA: ASP), 265
Mitra, D., & Rankin, J. M. 2002, ApJ, 577, 322
Mitra, D., & Seiradakis, J. H. 2004, in Hellenic Astronomical Society Sixth Astronomical Conference, The Effect of Aberration on Polarization Position Angle of Pulsars, ed. P. Laskarides (Athens: Univ. Athens), 205
Radhakrishnan, V., & Cooke, D. J. 1969, Astrophys. Lett., 3, 225
Radhakrishnan, V., & Rankin, J. M. 1990, ApJ, 352, 258
Ramachandran, R., & Kramer, M. 2003, A&A, 407, 1085
Rankin, J. M. 1983, ApJ, 274, 333
Rankin, J. M. 1990, ApJ, 352, 247
Rankin, J. M. 1993, ApJS, 85, 145
Ruderman, M. A., & Sutherland, P. G. 1975, ApJ, 196, 51
Sturrock, P. A. 1971, ApJ, 164, 229
Thomas, R. M. C., & Gangadhara, R. T. 2007, A&A, 467, 911
Thomas, R. M. C., & Gangadhara, R. T. 2010, A&A, 515, 86
Thomas, R. M. C., Gupta, Y., & Gangadhara, R. T. 2010, MNRAS, 406, 1029
You, X. P., & Han, J. L. 2006, Chin. J. Astron. Astrophys., 6, 237